A Facile and Mild Synthesis of 1-D ZnO, CuO, and α-Fe_2O_3 Nanostructures and Nanostructured Arrays

Hongjun Zhou[†] **and Stanislaus S. Wong**[†,‡,*]

[†]Department of Chemistry, State University of New York at Stony Brook, Stony Brook, New York 11794-3400, and [‡]Condensed Matter Physics and Materials Science Department, Brookhaven National Laboratory, Building 480, Upton, New York 11973

ABSTRACT ZnO nanowires, CuO nanowires, and α-Fe_2O_3 nanotubes as well as their corresponding arrays have been successfully synthesized *via* a low cost, generalizable, and simplistic template method. Diameters of one-dimensional (1-D) metal oxide nanostructures (~60−260 nm), measuring micrometers in length, can be reliably and reproducibly controlled by the template pore channel dimensions. Associated vertically aligned arrays have been attached to the surfaces of a number of geometrically significant substrates, such as curved plastic and glass rod motifs. The methodology reported herein relies on the initial formation of an insoluble metal hydroxide precursor, initially resulting from the reaction of the corresponding metal solution and sodium hydroxide, and its subsequent transformation under mild conditions into the desired metal oxide nanostructures. Size- and shape-dependent optical, magnetic, and catalytic properties of as-prepared 1-D metal oxides were investigated and noted to be mainly comparable to or better than the associated properties of the corresponding bulk oxides. A plausible mechanism for as-observed wire and tube-like motifs is also discussed.

KEYWORDS: nanowire · nanotube · template · array · zinc oxide · copper oxide · hematite

*Address correspondence to sswong@notes.cc.sunysb.edu, sswong@bnl.gov.

Received for review December 17, 2007 and accepted March 31, 2008.

10.1021/nn700428x CCC: $40.75

Though carbon nanotubes are the best known examples of one-dimensional (1-D) systems, the synthesis and characterization of metal oxide nanotubes and nanowires are equally critical because of the intrinsic importance of 1-D structures as model systems for the efficient transport of electrons and optical excitations.[1,2] The quantum confinement and low-dimensionality inherent to these systems allow for the generation of materials with unique properties, such as a higher luminescence efficiency[3] and a lowered lasing threshold[4] as compared with the bulk. Moreover, 1-D systems can be used as building blocks for the next generation of nanoscale optical, electronic, photoelectrochemical, and photovoltaic devices.[5,6] A lot of effort has been expended in overcoming numerous challenges associated with the efficient design of 1-D materials possessing well-defined and reproducible size, shape, monodispersity, purity, chemical composition, and crystallinity.[7] The binary oxides of transition metal elements, such as Zn, Cu, and Fe, in particular, represent one of the most diverse classes of materials with important size-dependent optical, electronic, thermal, mechanical, chemical, and physical properties, with a wide range of correspondingly diverse applications, including energy storage and sensing.[8−15]

ZnO is a key, II−VI compound semiconductor, with particularly attractive properties such as a direct wide band gap (3.37 eV), a large exciton binding energy (60 meV at room temperature), and an exciton Bohr radius in the range of 1.4−3.5 nm.[16] Moreover, ZnO possesses a high breakdown voltage, good piezoelectric characteristics, biocompatibility, as well as high mechanical, thermal, and chemical stability. All of these favorable properties render this material highly versatile for a host of optoelectronic applications including room-temperature ultraviolet lasers,[6] photodetectors,[17,18] dye-sensitized solar cells,[12,19] and field-effect transistors.[20−22] Moreover, the generation of high-quality, high aspect ratio, and high surface area ZnO nanowires as well as their corresponding assembly into functional arrays is expected to improve the luminescence efficiency of electro-optic devices and the sensitivity of chemical sensors. ZnO nanowire arrays have already been utilized as field emission sources as well as power generators for nanoscale devices.[23−25]

ZnO nanowires and nanowire arrays have been previously synthesized *via* both vapor and solution phases. Typical approaches were based on metal−organic chemical vapor deposition (MOCVD),[26,27] chemical vapor transport (CVT),[28,29] and pulsed laser deposition (PLD).[30] These methods, while fully capable of generating high-quality wires and arrays, do possess limitations. For instance, gas-phase methods tend to involve the use of high temper-

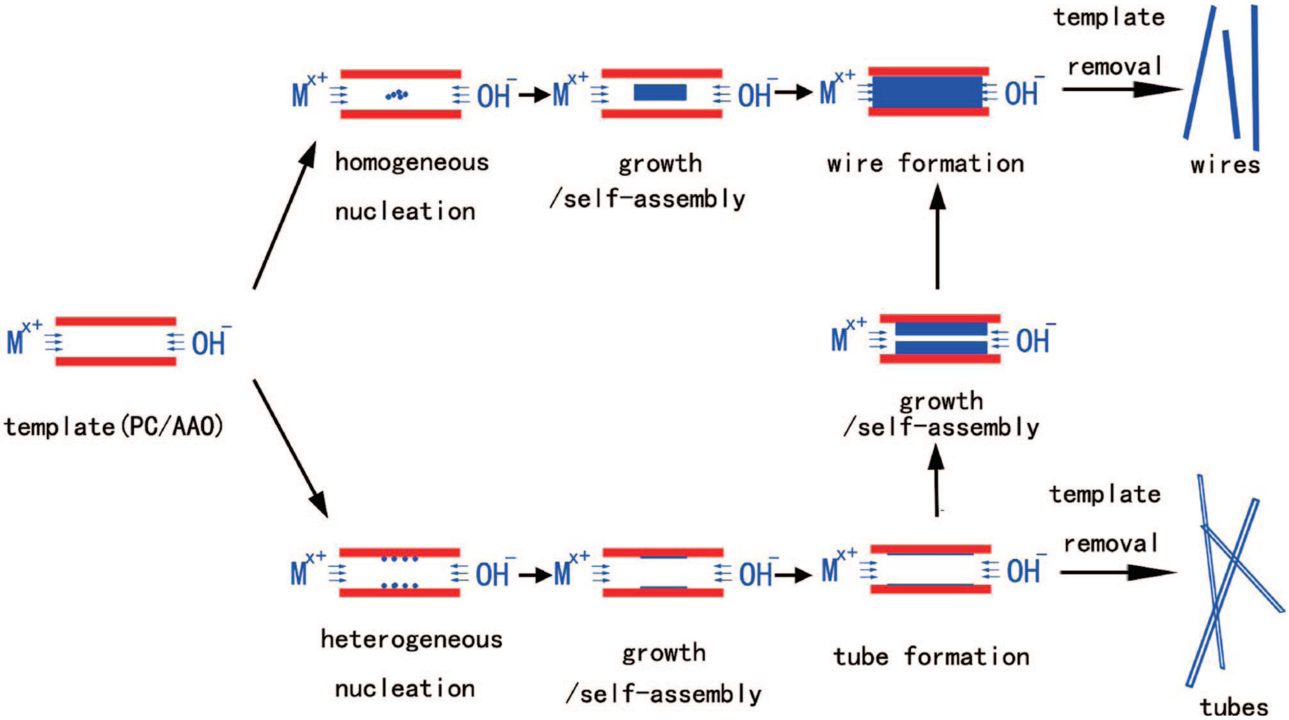

Scheme 1. Postulated mechanism for synthesizing nanowires and nanotubes from template pores, based on plausible explanations using heterogeneous and homogeneous processes.

atures (*e.g.*, 450−900 °C), potentially toxic precursors, and a very limited range of substrates in order to induce and direct the growth of ZnO nanowires. Moreover, PLD is not an inexpensive method of producing ZnO nanostructures. Solution-based methodologies also exist for ZnO formation.[31] As an illustrative example, layers of ZnO seed nanocrystals, measuring 5−10 nm in diameter, can be initially formed onto a Si substrate by thermally decomposing zinc acetate at 200−350 °C, and this 50−200 nm film of crystal seeds can be subsequently grown into vertical nanowire arrays at 90 °C.[32,33] Recently, Wang *et al.*[24] extended this methodology to the growth of aligned ZnO nanowire arrays on a plastic film using Au nanocrystal seeds.

As a *p*-type semiconductor with a narrow band gap (1.2 eV), CuO is a candidate material for photothermal and photoconductive applications.[34,35] Moreover, it is also an effective heterogeneous catalyst[36] for converting hydrocarbons completely into carbon dioxide and water. In addition, it is potentially a useful component in the fabrication of sensors, magnetic storage media, field emitters, lithium−copper oxide electrochemical cells, cathode materials, and high T_c-superconductors.[37,38] CuO nanowires can, for instance, be synthesized merely by heating Cu substrates in air from 400 to 700 °C,[34,39] while 1D CuO nanostructures can be obtained by a high-temperature transformation of their 1D copper hydroxide nanoscale analogues.[40−44] Polycrystalline CuO nanofibers have been prepared through electrospinning.[45] Free standing CuO nanotube and nanowire arrays have been fabricated by depositing precursors of either a MOCVD process[46] or a sol−gel technique[47] into the uniform pores of alumina templates, followed by subsequent annealing.

Because of its high stability, relatively low cost, and *n*-type semiconducting properties with a small bandgap (2.1 eV), α-Fe_2O_3 has been associated with applications ranging from gas sensing, lithium-ion battery production, catalysis, water splitting, water purification, and solar energy conversion to pigmentation.[14,48,49] Nanobelts, nanowires, and arrays of hematite structures have been synthesized by different methods, such as (a) the direct thermal oxidation of a pure iron substrate in an oxidizing atmosphere with a temperature range of 500−800 °C;[50,51] (b) the vacuum pyrolysis of β-FeOOH nanowires in a pressure range of 10^{-2} to 10^{-3} atm;[52,53] and (c) PLD using pressed Fe_3O_4 powder as a target.[54] Hematite nanotubes[14] and their corresponding arrays[55] have also been obtained by decomposing organometallic iron precursors, embedded within the pores of an alumina template, at high temperature. Moreover, hematite nanotubes have been synthesized by using carbon nanotubes as a structural template motif.[13]

Focus of Current Work. It is obvious based on all of the prior work that it would be desirable to develop a protocol that allows for an environmentally sound and cost-effective methodology of metal oxide nanoscale synthesis without the need to sacrifice on sample quality, crystallinity, monodispersity, and purity. That is, it would be a viable, complementary advance to develop a generalizable protocol aimed at ZnO, CuO, and α-Fe_2O_3 (hematite) nanowire/array

TABLE 1. Effect of Parameter Selection on Preparation of Metal Oxide 1-D Nanostructures at a Constant Overall Reaction Time of 1 h. Measured 1-D Nanostructure Widths (*W*) Are Dependent on Corresponding Pore Dimensions of Templates Used

sample	metal salts used	basic solution	concn of base (M)	temp (°C)	template	observed product morphology (width, *W*; length, *L*; diameter, *D*)
A	Zn^{2+}	NaOH	0.1	80	polycarbonate	ZnO nanowires. *W*: 60 ± 10 nm. *L*: 2−4 μm
B	Zn^{2+}	NaOH	0.1	80	polycarbonate	ZnO nanowires. *W*: 120 ± 20 nm. *L*: 2.5−5 μm
C	Zn^{2+}/Cu^{2+}	NaOH	0.1	80	polycarbonate	ZnO/CuO nanowires. *W*: 250 ± 50 nm. *L*: 10−15 μm
D	Zn^{2+}/Cu^{2+}	NaOH	0.01	80	polycarbonate	ZnO/CuO nanowires. *W*: 250 ± 50 nm. *L*: 1−2 μm ZnO/CuO nanoparticles. *D*: 90 ± 30 nm
E	Zn^{2+}/Cu^{2+}	NaOH	0.1	room temp	polycarbonate	$Zn(OH)_2/Cu(OH)_2$ nanowires. *W*: 250 ± 50 nm. *L*: 4−8 μm
F	Zn^{2+}/Cu^{2+}	$NH_3 \cdot H_2O$	0.01	room temp	polycarbonate	$Zn(OH)_2/Cu(OH)_2$ nanoparticles. *D*: 90 ± 30 nm
G	Zn^{2+}/Cu^{2+}	$NH_3 \cdot H_2O$	0.01	room temp	alumina	$Zn(OH)_2/Cu(OH)_2$ nanoparticles. *D*: 90 ± 30 nm
H	Fe^{3+}	$NH_3 \cdot H_2O$	0.01	room temp	alumina	$Fe(OH)_3$ nanotubes. *W*: 300 ± 50 nm. *L*: 3−9 μm
I	Fe^{3+}	$NH_3 \cdot H_2O$	0.1	room temp	alumina	$Fe(OH)_3$ nanotubes. *W*: 300 ± 50 nm. *L*: 4−12 μm
J	Fe^{3+}	$NH_3 \cdot H_2O$	0.01	(a) room temp; (b) annealing to 600 °C	alumina	α-Fe_2O_3 nanotubes. *W*: 260 ± 6 nm. *L*: 3−9 μm
K	Fe^{3+}	NaOH	0.1	80	polycarbonate	amorphous Fe_2O_3 (or β-FeOOH) nanowires. *W*: 250 ± 50 nm: *L*: 4−5 μm
L	Fe^{3+}	$NH_3 \cdot H_2O$	0.01	room temp	polycarbonate	$Fe(OH)_3$ nanoparticles. *D*: 100 ± 20 nm

formation aimed at overcoming either the high-temperatures, the need for expensive equipment, the use of potentially toxic precursors and byproducts, or the ultimate product polycrystallinity, characteristic of previous literature methods of metal oxide nanoscale synthesis.

In our group, we have modified and refined the conventional template-directed synthesis, popularized by Charles Martin's group,[56−58] to yield a relatively simple and versatile variation with which to prepare size-controlled, one-dimensional nanostructures under ambient conditions in aqueous solution with reliable control over shape, dimensionality, and crystallinity. We have previously demonstrated[59] the room-temperature preparation of single-crystalline $BaWO_4$ and $BaCrO_4$ nanowires with different controllable sizes as well as the creation of arrays of these nanowires in the pores of an alumina membrane. We have subsequently extended this methodology to the production of BaF_2, CaF_2, and SrF_2, in addition to NH_4MnF_3 and $KMnF_3$ nanowire structures.[60] The gist of the method is that we initially mount conventional, commercially available membranes, composed of either alumina or polymer, between the two halves of a glass U-tube cell.[61,62] The half-cells are then filled with equimolar solutions of precursor solutions. In effect, the pores in the membranes are used as the environment with which to confine and control the growth of our one-dimensional products. Moreover, these as-produced nanomaterials are chemically pure, are structurally well-defined, and can be generated in reasonable quantities.

The key point is that our method is generalizable and can be adapted to the production of binary metal oxides, which are the focus of our efforts herein. As an example of the potential of our strategy, we have used polycarbonate (PC) templates to synthesize ZnO nanowires and their corresponding arrays. By comparison with previous techniques discussed for ZnO nanostructure synthesis (for which similar arguments can be analogously made for CuO as well as for α-Fe_2O_3 nanostructures), the key attractive attributes of our methodology are (1) use of relatively low temperature (*i.e.*, room temperature to about 80 °C); (2) short reaction time (about 30 min); (3) simplistic, inexpensive experimental setup, requiring the use of a homemade U-tube; (4) lack of either a toxic organic precursor or a toxic byproduct (in fact, we only utilized an inorganic metal salt solution along with sodium hydroxide in our synthesis); (5) relative ease of template removal by immersion in methylene chloride; (6) no need for either ZnO or metal nanocrystalline "nucleation seeds"; and finally, (7) substrate-less generation of ZnO nanowire arrays.

What is highly significant is that the last point implies that ZnO (or frankly any other metal oxide such as CuO and α-Fe_2O_3) arrays can be theoretically transferred onto any type of substrate, be it curved, linear, rigid or pliant, upon template attachment to a conductive tape and subsequent template removal. This potential for highly flexible array generation will have relevance for applications as diverse as usage in portable electronics, implantable biosensors, biodetectors, and self-powered electronic devices.[24]

RESULTS AND DISCUSSION

In the experimental setup in these experiments, the contents of each solution in either half of the U-tube are allowed to diffuse toward each other across a wetted template membrane physically separating the two halves (Supporting Information, Figure S1). Hence, metal cations and hydroxide anions will meet at the interface, react in a hydrolysis process, and nucleate the formation of the corresponding hydroxides. These in-

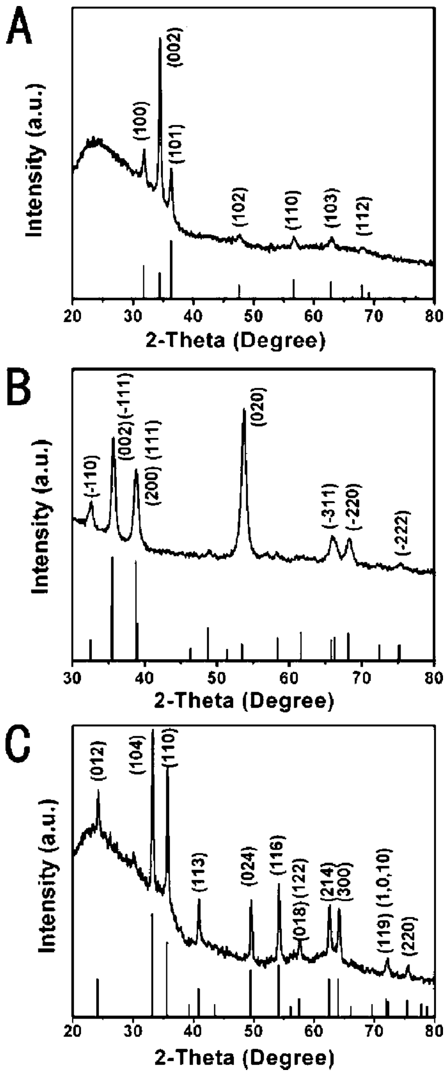

Figure 1. XRD patterns of as-prepared samples: (A) ZnO nanowires, (B) CuO nanowires, and (C) α-Fe_2O_3 nanotubes. Representative diffraction patterns (upper half) and corresponding standard JCPDS diffraction patterns (lower half) for each of the samples are shown in each figure part.

TABLE 2. Crystallographic Data of as-Prepared Samples and Comparisons with Expected Literature Values

sample	JCPDS database No.	phase (space group)	calculated constants	literature values
ZnO nanowires	36-1451	Hexagonal (*P63mc*)	$a = 0.3249$ nm	$a = 0.3249$ nm
			$c = 0.5206$ nm	$c = 0.5206$ nm
CuO nanowires	45-0937	Monoclinic (C2/*c*)	$a = 0.4685$ nm	$a = 0.4685$ nm
			$b = 0.3426$ nm	$b = 0.3425$ nm
			$c = 0.5130$ nm	$c = 0.5130$ nm
α-Fe_2O_3 nanotubes	33-0664	Rhombohedral (*R*3*c*)	$a = 0.5036$ nm	$a = 0.5035$ nm
			$c = 1.3749$ nm	$c = 1.3740$ nm

soluble hydroxides will begin to precipitate from solution, once the supersaturation value, which is rather low based on the magnitudes of the solubility product constants of these materials, shown in Table S1, for their production has been exceeded. We offer a plausible scenario (Scheme 1) for the initial metal hydroxide nanostructure formation observed herein.

Mechanistic Insights. If the interactions between reagent molecules are stronger than those between the reagent molecules and the pore walls, the nucleation process and accompanying product formation will tend to happen within the voluminous confines of the pores themselves in a homogeneous-type process. That is, single crystals of nanoscale metal hydroxides therefore derive from isolated, disparate nucleation sites, which then grow by extension throughout the porous network. Continued growth then occurs at the particle surface at a rate limited by ion availability, until the crystal impinges on the template surface itself, which ultimately limits further particle growth. Within the cylindrical confines of the template pores, as-formed particles in this scenario essentially self-assemble with each other into either *wire-like or rod-like motifs*.

On the other hand, if the interactions between the reagent molecules are weaker than those between the reagent molecules and the pore walls, the nucleation and accompanying growth processes may tend to be localized at the surfaces of the pore walls in a heterogeneous-type process. Such a process may occur, for instance, if the pore wall is positively charged while the reagent particles are negatively charged. This preferential confinement of growth to the inherent geometry of the pore walls can therefore lead to the generation of primarily *tube-like motifs* upon the elongation and assembly of the as-formed particles. Such a scenario has been previously noted in the case of polymeric microtubules formed in templates, wherein nascent polymer chains initially adsorbed to the pore walls yielding a thin polymer "skin", that became thicker with time until it was quenched with water.[61]

With continued reaction, nanowire formation can be visualized as a lateral thickening of the tubular structure, which, as further supply of precursors to the inside is blocked by the ever-growing tube thickness coupled with an ever-decreasing inner tube diameter, eventually constricts the entire porous interior of the template, filling it completely. In other words, continued growth of the nanotubes is limited only by reagent ion availability and diffusivity as well as by intrinsic geometrical constraints imposed by the template channels. Hence, nanowires are considered as the ultimate limit of nanotube growth, at least in terms of its width. This hollow nanotube-to-solid nanowire transformative mechanism has been previously proposed with respect to the synthesis of TiO_2 nanotubes and nanowires within alumina (AAO) templates.[63] It should be noted that concentration and temperature are also expected to govern the morphologies of the resulting nanotubes and nanowires with lower concentrations and temperatures expected to favor short, hollow nanotubes, while high concentrations and temperatures are expected to lead to the growth of longer, thicker wires.

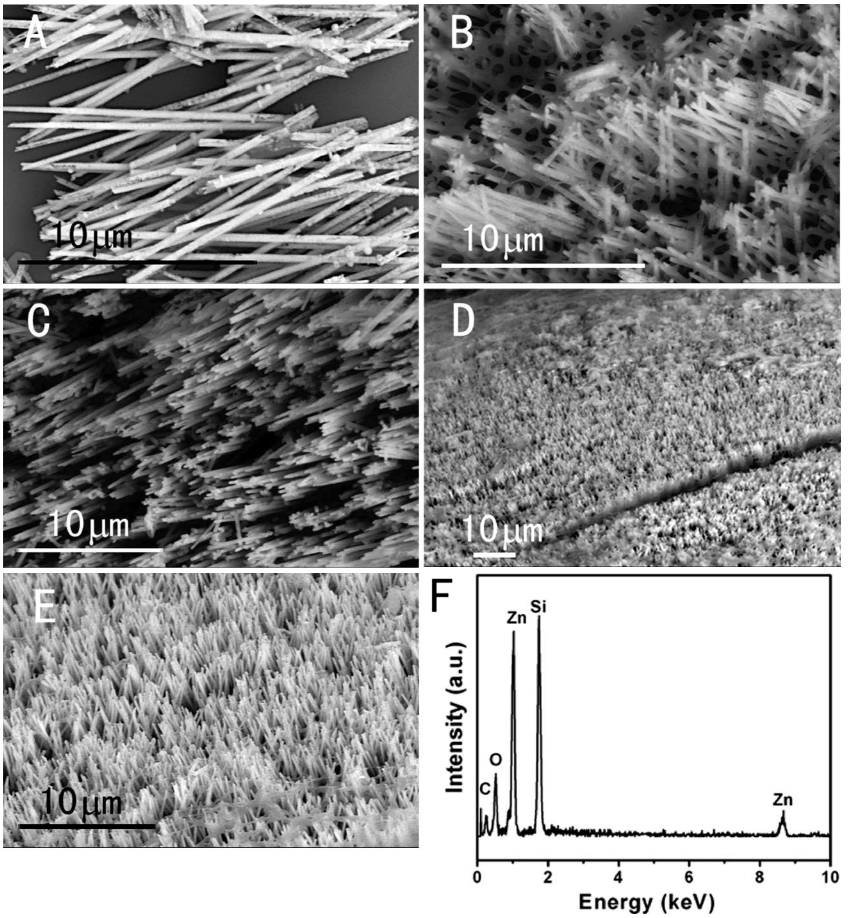

Figure 2. SEM images of (A) isolated ZnO nanowires and (B) ZnO nanowires embedded in the template; (C−E) additional SEM images of ZnO nanowire arrays after removal of the template; representative EDS pattern (F) of as-prepared ZnO nanowires and arrays.

In support of this mechanism, we have performed a systematic series of experiments (Table 1) to probe the effect of parameters such as (a) temperature and (b) concentration on the resulting nanostructure morphology. The importance of temperature cannot be minimized. In fact, chemically pure, crystalline nanoscale ZnO and CuO samples (*e.g.*, samples A and B from Table 1) upon template removal, were obtained only when the U-tube experimental setup itself was heated to 80 °C. It is plausible to assume that a higher temperature accelerates ion diffusion rates across the template. Hence, we ran our U-tube experiments at room temperature as a comparison. In terms of the concentration parameter, we varied the concentration of OH^-, necessary to induce precipitation, in our experiments from 0.01 to 0.1 M with higher concentrations (and therefore fluxes) of hydroxide ion expected to foster particle nucleation as well as nanostructure elongation. It should be noted though that the effect of changing this variable is slightly more nuanced as local, dynamic concentrations of hydroxide within the template environment are dependent on diffusion rates as well.

According to our mechanistic discussion, a higher temperature and/or a higher base concentration should promote high diffusion rates and correspondingly high local concentrations of interacting reagent ions. These conditions should therefore lead to initial particle formation followed by subsequent aggregation, coalescence, and self-assembly of these constituent particles to yield either nanowires or nanotubes. This prediction is borne out by the production of sample C, created at the highest temperature and base concentration used, wherein the ZnO and CuO generated consisted solely of nanowires. Conversely, upon reduction of either base concentration (sample D) or temperature (sample E), shorter nanowires (a few micrometers in length *versus* tens of micrometers in length for sample C) were obtained and in some cases, isolated particles were also generated in addition to the wire-like motifs. Simultaneous decreases in both temperature and base concentration yielded only small, discrete particles of likely either $Zn(OH)_2$ or $Cu(OH)_2$, measuring tens of nanometers (sample F and G), irrespective of the template used (*e.g.*, PC or alumina), suggesting that for these two materials in particular, the nucleation and growth processes were essentially homogeneous in nature.

The case of iron oxide nanostructure formation in the presence of an alumina template is clearly different as heterogeneous processes likely predominate. That is, the reagent particle-pore wall interaction was comparatively strong and nucleated particles assembled primarily into tubular motifs. For instance, even under the mildest of experimental conditions, for example at very low concentrations of ammonium hydroxide (0.01 M) and at room temperature, 1D iron-containing nanotubes (likely $Fe(OH)_3$) were synthesized, as shown in sample H. The fact that under similar conditions, we could not generate 1D nanostructures of either zinc hydroxide or copper hydroxide suggests that the significantly smaller K_{sp} value ($\sim 10^{-40}$; Table S1) of $Fe(OH)_3$, as compared with the relatively higher K_{sp} values ($\sim 10^{-20}$; Table S1) for $Cu(OH)_2$ and $Zn(OH)_2$, was highly conducive to iron hydroxide nanostructure formation. Increasing the concentration of ammonium hydroxide to 0.1 M while maintaining the reaction temperature constant (sample I) led to the generation of longer $Fe(OH)_3$ nanotubes, which might have arisen owing to higher local concentrations of reactive reagent ions, which is again consistent with our mechanism; in fact, it was only with an additional annealing step to 600 °C that one could successfully syn-

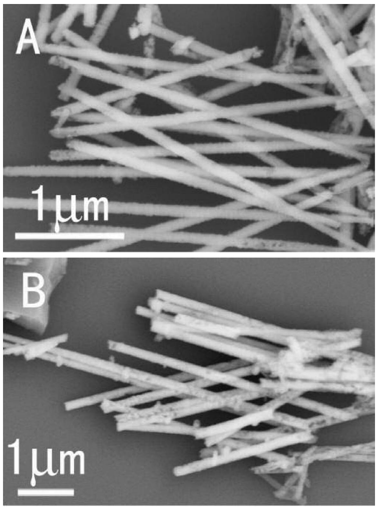

Figure 3. Collection of SEM images of ZnO nanowires prepared from a PC template possessing pore sizes of (A) 50 nm and (B) 100 nm, respectively.

thesize hematite nanotubes (sample J). By contrast, increasing both the reaction temperature (to 80 °C) and hydroxide concentration (to 0.1 M) as well as reverting to a PC template (sample K) resulted in the formation of iron-containing, nonhematite nanowires, as we will subsequently describe in our XRD data discussion. The presence of the filled nanowire structures within the PC template reflected the more favorable reagent particle−particle *versus* particle−pore wall interaction in this pore environment. Hence, iron oxide nanowire growth in PC templates is analogous to the homogeneous processes described for Zn and Cu. Such an assertion was further confirmed by the formation of sample L, prepared under low-temperature and low concentration conditions. As with sample F by analogy, only small, discrete particles, measuring about 100 nm in diameter and likely consisting of either amorphous hematite or more likely, iron hydroxide, were obtained.

X-Ray Diffraction. On the basis of this knowledge base, in the remainder of the paper, we focus on the characterization and manipulation of ZnO, CuO, and α-Fe_2O_3 1-D samples, optimally prepared by experimental conditions associated with samples A, B, C, and J (Table 1). We have demonstrated in principle that, with our technique, isolated 1D metal oxides of essentially any diameter can be obtained with templates of arbitrary pore size. The reason we mainly focus on samples prepared using 200 nm templates is due to our ability to generate sufficiently large quantities of these nanoscale materials to enable a more facile data interpretation of their unique properties.

The purity and crystallinity of as-prepared metal oxide nanostructure samples were initially examined by powder XRD measurements (Figure 1). As shown in Table 2, all peaks of as-prepared samples can be readily indexed to pure phases of our desired materials. No detectable impurities were noted in any of the patterns. Thus, we were able to obtain hexagonal-phase ZnO and monoclinic-phase CuO crystals at 80 °C without the necessity of an additional annealing step at high temperature.

By contrast, for the production of rhombohedral-phase Fe_2O_3, under identical experimental conditions (use of a polycarbonate (PC) template, at 80 °C, same concentrations of precursors), the XRD pattern of the as-prepared sample (which incidentally was composed of 1D nanowire-like structures (sample K, Table 1) upon further analysis) was completely featureless. This diffraction result suggested that either little if any Fe_2O_3 crystals were produced or the as-prepared sample was effectively amorphous. Hence, we hypothesized that further annealing was likely needed to increase sample crystallinity. However, since the PC template could only be used below 140 °C beyond which it would either deform, melt, or even decompose, the use of an AAO template was substituted. Resultant samples (in AAO) were annealed at 600 °C for 1 h. An XRD pattern (Figure 1C, upper curve) showed that hematite (α-Fe_2O_3) crystals (sample J, Table 1) could therefore be obtained, as planned.

Electron Microscopy. The morphology of as-synthesized one-dimensional samples was studied using FE-SEM and TEM. Figure 2A shows SEM images of as-prepared ZnO nanowires (sample C, Table 1), isolated from a 200 nm PC template. Diameters of these ZnO nanowires are about 250 ± 50 nm, whereas the associated lengths measure about 10 ± 1 μm. Additional images of ZnO nanowires (samples A and B, Table 1), grown in templates with pore diameters measuring 50 and 100 nm, respectively, are presented in Figure 3. The diameters of these particular ZnO nanowires are 60 ± 10 and 120 ± 20 nm, respectively, consistent with the pore size dimensions of the originating templates themselves. Figure 2B shows an image of samples with the template partially removed and with individual, aligned ZnO nanowires protruding vertically from the inner surfaces of the template pores. In this architecture, nanowire arrays are structurally supported by the presence of the remnant PC template which thereby increased the overall strength of the composite structure. This is significant because it is known that the power-generating capability of polymer-supported ZnO nanowire arrays is higher than that of corresponding arrays lacking any such mechanical support.[24] In our experiments, arrays of ZnO nanowires appear to be structurally robust and well preserved, after careful and complete removal of the entire PC template by methylene chloride, as shown in Figure 2C (top view) and in Figure 2D,E (tilt view). The EDS spectrum (Figure 2F) shows the presence of Zn and O, as expected with the Si signal at-

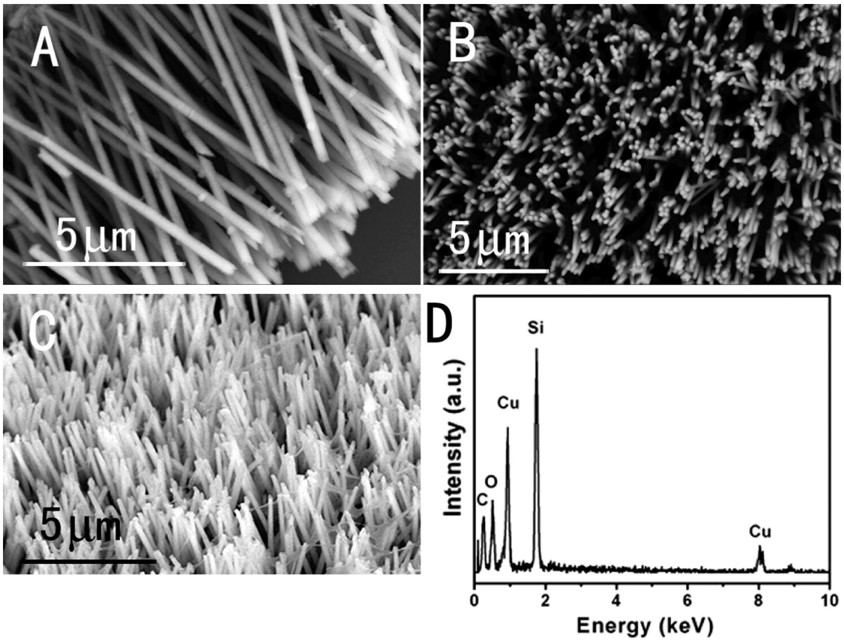

Figure 4. SEM image of (A) isolated CuO nanowires; (B, top-view; C, tilt-view) SEM images of arrays of CuO nanowires after template removal; representative EDS pattern (D) of as-prepared CuO nanowires and associated nanowire arrays.

tributable to the underlying Si wafer used for imaging.

By analogy to ZnO, SEM data on isolated CuO nanowires are shown in Figure 4A. Diameters and lengths are 250 ± 50 nm and 12 ± 2 μm, respectively. CuO nanowire arrays were also prepared in an analogous fashion to that of ZnO, that is, upon removal of the PC template, as shown in Figure 4 panels B and C. The EDS spectrum (Figure 4D) confirms the existence of Cu and O with the presence of Si attributable to the underlying Si wafer used for microscopy imaging.

As opposed to nanowires, hollow α-Fe_2O_3 nanotubes were obtained using AAO as the reaction template (Figure 5A). Diameters and lengths of the as-obtained nanotubes measured approximately 260 ± 60 nm and 6 ± 3 μm, respectively. The existence of short nanotubes may arise from breakage of long nanotubes during the associated sonication process for TEM sample processing. Upon removal of a thin layer of AAO template, nanotubes can be clearly observed, growing within the pores of the template (Figure 5B). However, it is evident that the nanotubes themselves are not actually attached to the inner surfaces of the pores. Shrinkage of the tubes toward the pore centers may have resulted from a loss of water upon annealing of $Fe(OH)_3$ (generated in situ from the reaction of $Fe_2(SO_4)_3$ and ammonium hydroxide) at high temperature. Arrays of aligned iron oxide nanotubes are shown in Figure 5C after careful removal of the AAO template. The EDS spectrum (Figure 5D) is consistent with the existence of Fe and O, whereas the Al signal originates from the remaining AAO template and the Si signal emanates from the Si wafer used in the imaging process. Additional SEM images of all of these metal oxide samples, highlighting the prevalence of the reaction, are shown in Figure S2.

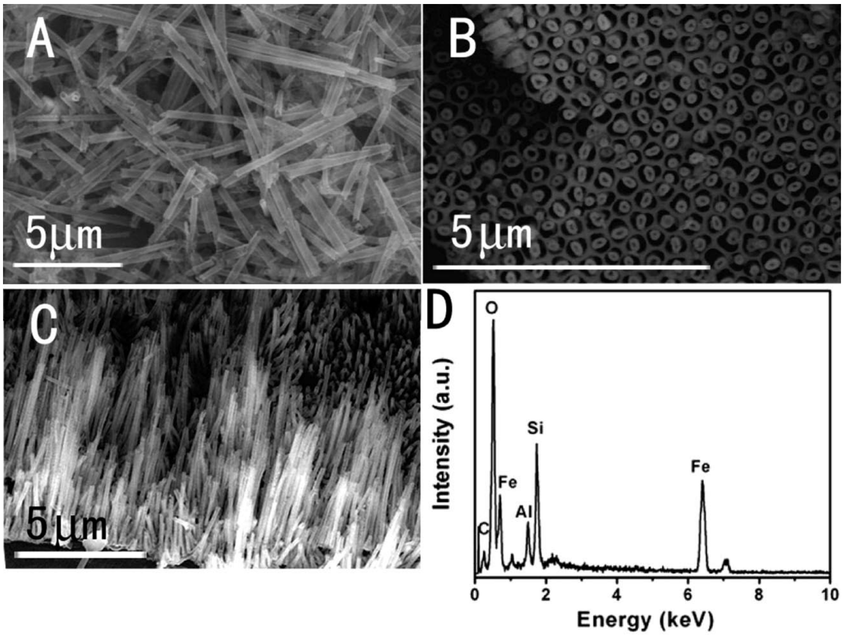

Figure 5. SEM image of (A) isolated α-Fe_2O_3 nanotubes; SEM images of arrays of α-Fe_2O_3 nanowires before (B, top-view) and after (C, tilt-view) template removal; representative EDS pattern (D) of as-prepared α-Fe_2O_3 nanotubes and arrays.

The morphology of all of the samples was also examined by low-magnification TEM as shown in Figure 6 panels A, C, and E as well as Figure S3. These images further confirm the range of sample diameters obtained from SEM data. All as-obtained nanowires and nanotubes are essentially uniform in terms of shape and morphology.

A high resolution TEM image (Figure 6B) and associated SAED pattern (inset to Figure 6B) taken on an individual ZnO nanowire show the single crystalline nature of the sample. The lattice spacing can be indexed to the (100) plane. SAED patterns obtained at different spots along the same nanowire were effectively identical and confirm that each ZnO nanowire is essentially uniform in composition and relatively devoid of impurities. By contrast, although a similar procedure was used to generate CuO nanowires, the resulting product was not single crystalline. That is, a HRTEM image (Figure 6D) of a CuO nanowire shows the presence of different crystalline domains and SAED (inset to 6D) confirms that it is polycrystalline. The lattice spacing of the crystal domain indexed corresponds to (−111). Moreover, our as-generated α-Fe_2O_3 nanotubes consist of many small but misoriented single-crystalline nanocrystalline domains (Figure 6E and F), rendering the entire structure as polycrystalline in nature (inset in Figure 6F). The lattice spacing taken from one of these single-crystalline particles has been ascribed to the (110) plane. Considering that these iron oxide structures were prepared using an annealing step at high temperature, this result is not altogether surprising.

We were also able to generate array structures of our nanowire samples. Our protocol allows for the transference of any type of metal oxide array motifs onto a nonspecific substrate, nonlinear or otherwise, using double-sided, conductive tape. As a demonstration of principle of our ability to pattern metal oxide nanowire arrays over macroscopically relevant areas, we attached CuO arrays onto curved substrates of varying chemical composition. Figure 7 panels A and B are SEM images of CuO arrays immobilized using conductive carbon tape onto a plastic tip, measuring 1.5 mm in outer diameter. Figure 7B corresponds spatially to the white square designated in Figure 7A and highlights the feasibility of generating vertically aligned metal oxide arrays at room temperature. Figure 7C and 7D (magnified view corresponding spatially to the white square shown in 7C) show the presence of CuO arrays immobilized onto a silica glass rod, measuring 0.8 mm in outer diameter, as mediated by the presence of conductive, copper tape. By analogy, ZnO arrays were attached onto an identical silica glass rod, as shown in Figure 7E and 7F (magnified view corresponding spatially to the white square shown in 7E), using conductive, copper tape. We noted that array integrity was even more highly preserved in the case of ZnO and CuO nanowire arrays, partly because methylene chloride, used to remove the PC template, is not as corrosive to the intrinsic structure of copper tape as it is to carbon tape.

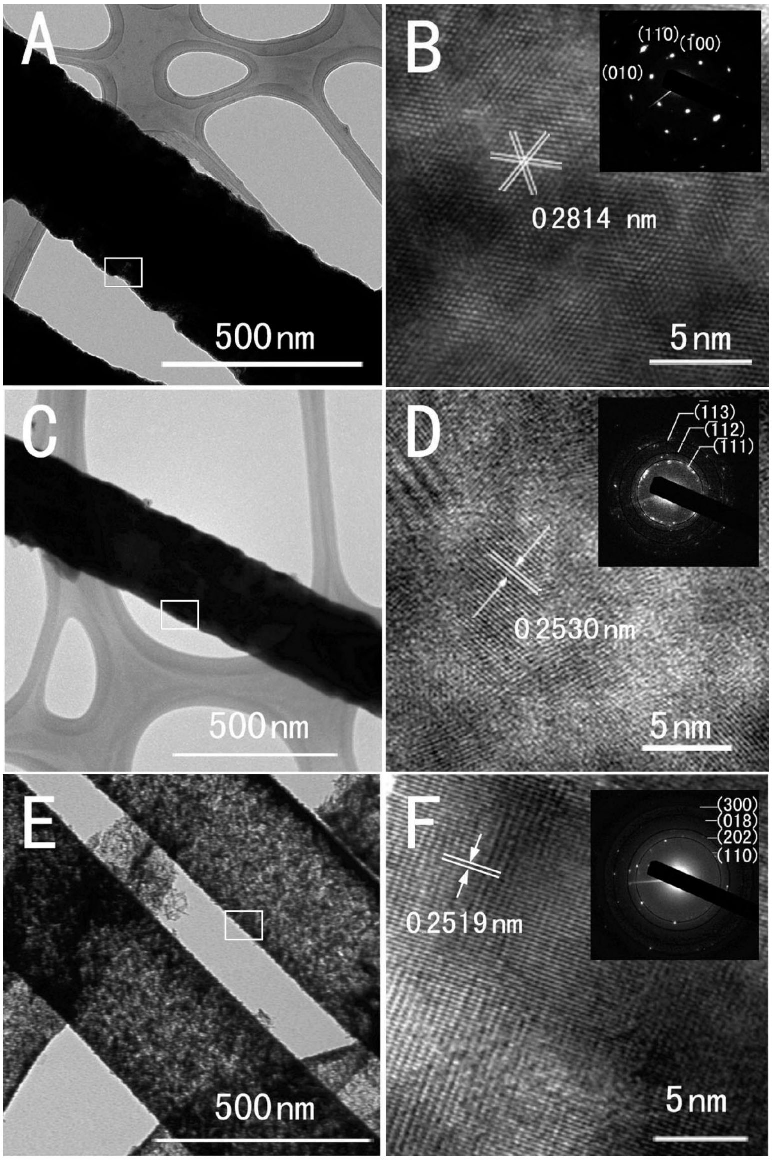

Figure 6. TEM (A, C, E) and HRTEM (B, D, F) images and corresponding SAED patterns (insets) of portions of ZnO nanowires (top), CuO nanowires (middle), and α-Fe_2O_3 nanotubes (bottom), respectively. Squares in panels A, C, and E highlight spatially specific locations on the various nanoscale oxide samples, where the HRTEM images were taken.

We emphasize that this technique, involving an initial nanoscale oxide nanowire formation inside a template followed by attachment to the desired substrate using conductive tape and subsequent template removal, is significant not only because this generalizable protocol can be performed under ambient conditions for essentially any type of material but also because this procedure can transfer arrays onto any type of substrate of any geometric configuration over a reasonably large macroscopic area, a capability which is technologically relevant. Moreover, the reported methodology is effectively independent of the mechanical deformability, melting behavior, and/or decomposition temperature of the substrate onto to which the arrays are transferred, and furthermore, it does not necessitate the use of catalytic seed particles, all of which are important factors in conventional methods traditionally associated with array patterning. We even possess the potential of attaching chemically distinctive types of metal oxide arrays in spatially adjacent positions onto a given substrate using our simplistic technique.

Optical Spectroscopy. Optical properties of as-prepared samples were also investigated. Figure 8 shows the UV−visible spectra of as-prepared samples. The absorp-

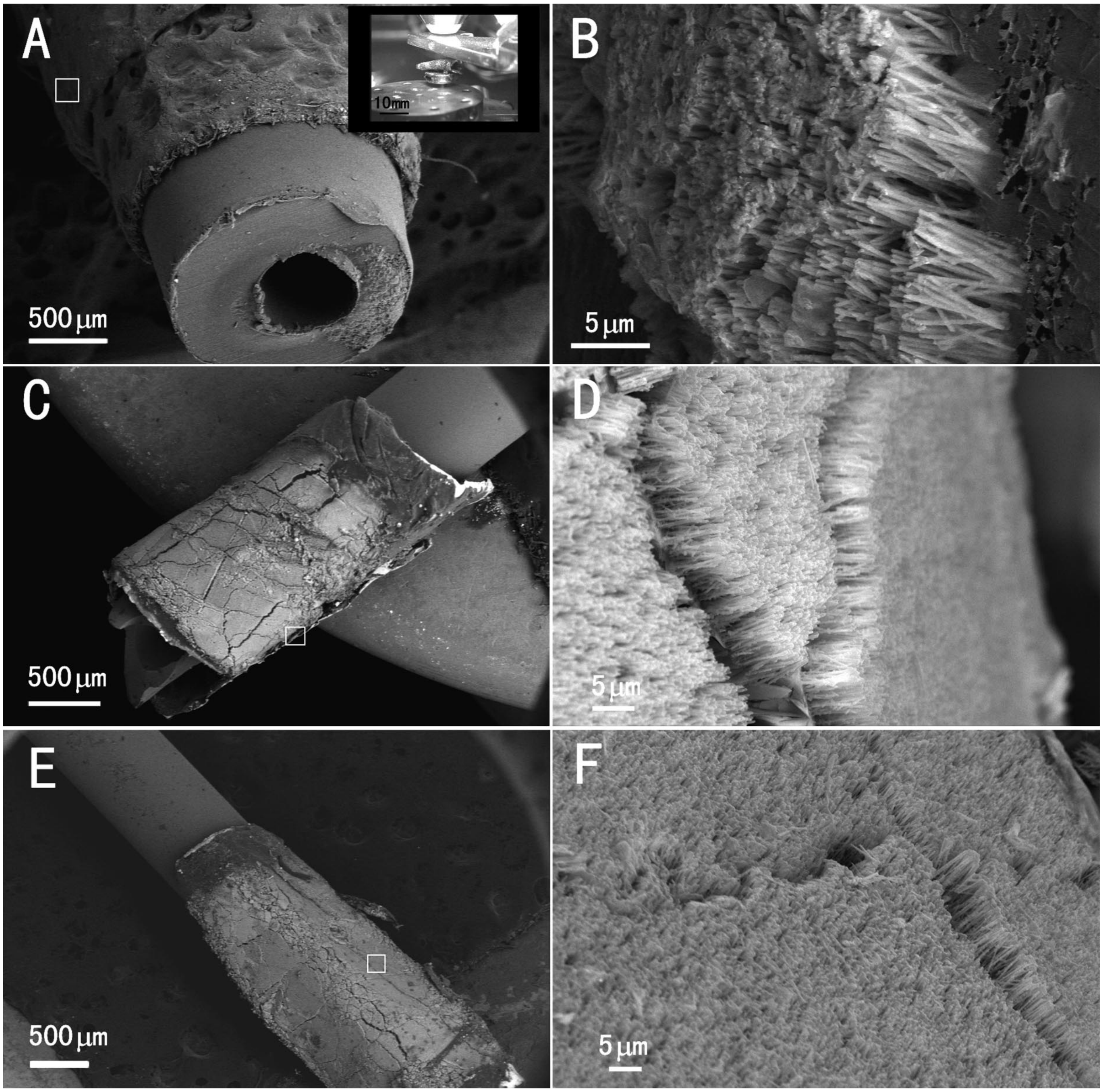

Figure 7. SEM images of CuO nanowire arrays immobilized onto (A and B) a plastic tip as well as onto (C and D) a curved glass rod. (E and F) Analogous SEM images of ZnO nanowire arrays immobilized onto a curved glass rod.

tion spectrum (Figure 8A) of the ZnO nanowires showed the presence of a maximum absorption peak at 364 nm, which blue-shifted relative to that of the corresponding signal for bulk ZnO, in agreement with prior work.[64,65] By analogy, the maximum absorption peaks of CuO nanowires and of α-Fe_2O_3 nanotubes (Figure 8B and 8C) were noted at 205 and 208 nm, respectively, which also showed a blue-shift relative to that of their bulk counterparts, consistent with previous reports.[66,67] Essentially, with decreasing sample size, the optical edge shifts to higher energy, a phenomenon attributable to quantum size and confinement effects.[68] Indeed, a size-dependent blue-shift has been observed in the absorption spectra of nanocrystalline motifs of many other bulk materials, such as TiO_2 nanowires.[69]

The room temperature photoluminescence (PL) spectrum of ZnO nanowires is shown in Figure 8D. A strong UV emission observed at ~380 nm most likely corresponds to near band-edge emission, while the presence of green emission at ~501 nm can be attributed to radiative recombination of photogenerated holes in the valence band with electrons in singly occupied oxygen vacancies.[32,70,71]

Moreover, evidence for the formation of metal oxides was provided by FT-IR spectra, shown in Figure S4. The broad absorption band around 500 cm^{-1} of the ZnO sample can be attributed to either the stretching mode of ZnO[64,72] or an oxygen vacancy defect complex[73,74] in that compound. By analogy, the maximum absorption band at around 520 cm^{-1} of the CuO sample corresponds to the broad stretching mode of CuO along the [101] direction.[75,76] Finally, for the α-Fe_2O_3 sample, the presence of bands located at 580 cm^{-1} and 485 cm^{-1} is consistent with the presence of A_{2u}/E_u and E_u vibrations, respectively.[77–79]

Magnetic Behavior. The magnetic behavior of as-prepared α-Fe_2O_3 nanotubes was investigated using SQUID analysis. Field-cooled and zero-field-cooled magnetization curves under 100 Oe are shown in Figure 9A. The magnetic phase transition from the canted ferromagnetic phase to another antiferromagnetically ordered state has been reported for bulk hematite samples to be around 260 K, characterized by a sharp decrease in the magnetization in the so-called Morin transition.[80] The magnetic behavior of our α-Fe_2O_3 nanotubes was different though. Our results are in agreement with analogous data observed for a hydrothermally prepared α-Fe_2O_3 nanotube sample,[81] as well as for spherical α-Fe_2O_3 nanoparticles.[82] For instance, for our template-prepared nanotubes, we observed a hysteresis loop at 5 K (Figure 9B), indicative of the presence of a coercive field at 245 Oe, characteristic of a soft magnet; by analogy, hydrothermally prepared nanotubes yielded a coercive field of 280 Oe.[81] These results are suggestive of a long-range magnetic ordering, suppressing the Morin transition. Moreover, it can be observed that our α-Fe_2O_3 nanotubes show a well-defined peak at 65 K, below which the magnetic moments of particles are frozen or blocked; by analogy, for spherical α-Fe_2O_3 nanoparticles, that blocking temperature was 45 K.[82] Our FC curve above the blocking temperature does not follow standard Curie−Weiss behavior, suggesting the presence of strong intertube interactions. As we cannot ascribe these behaviors to any magnetic impurities in our samples, our overall observations herein can potentially be assigned to structural disorder, such as the presence of small crystalline particulate regions, an assertion supported by the polycrystalline nature of our iron oxide tubes, as evidenced by the TEM/HRTEM images in Figure 6E,F. In addition, morphology, finite size, and surface effects are additionally important factors, since hematite nanocubes[66] also behave magnetically distinctively as compared with the bulk.

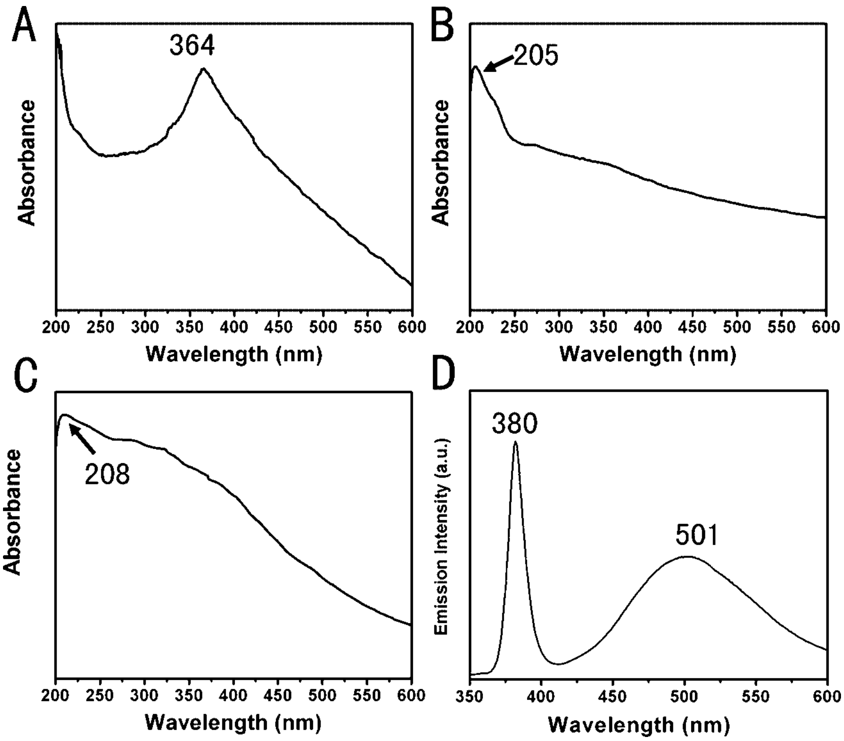

Figure 8. UV−visible spectra of as-prepared (A) ZnO nanowires, (B) CuO nanowires, and (C) α-Fe_2O_3 nanotubes; (D) photoluminescence spectrum of ZnO nanowires (excitation wavelength of 325 nm).

Photocatalytic Measurements. Semiconductor-assisted photocatalysis and photo-oxidation of organic contaminants, as exemplified by model organic systems, remain as reasonable methodologies for converting pollutants into relatively harmless byproducts. The photocatalytic potential of as-prepared ZnO nanowires was evaluated by measuring the absorption intensity of methyl orange at 464 nm upon photoexcitation with UV light at 366 nm. Our data clearly show that nanowires and nanoparticles as well as the bulk sample of ZnO are active photocatalysts, as illustrated in Figure

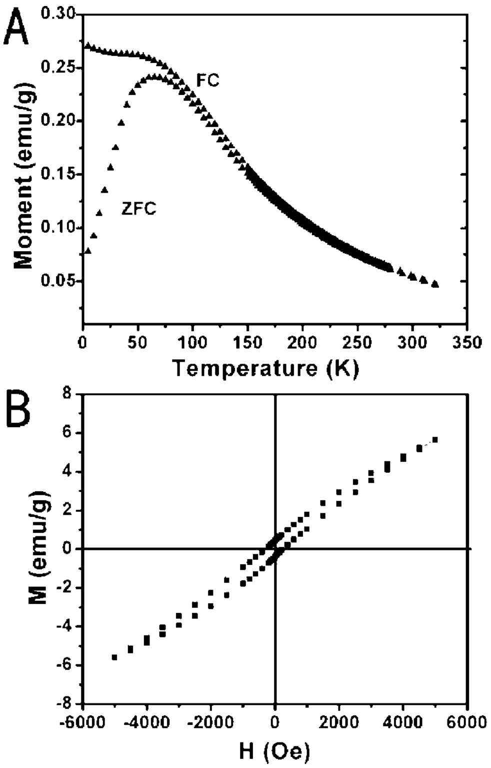

Figure 9. (A) Temperature dependence of the magnetic susceptibility for α-Fe_2O_3 nanotubes, showing zero field cooling (ZFC) and field cooling (FC) curves, with an applied magnetic field set at 100 Oe; (B) hysteresis loop at 5 K revealing the coercivity of as-prepared hematite nanotubes.

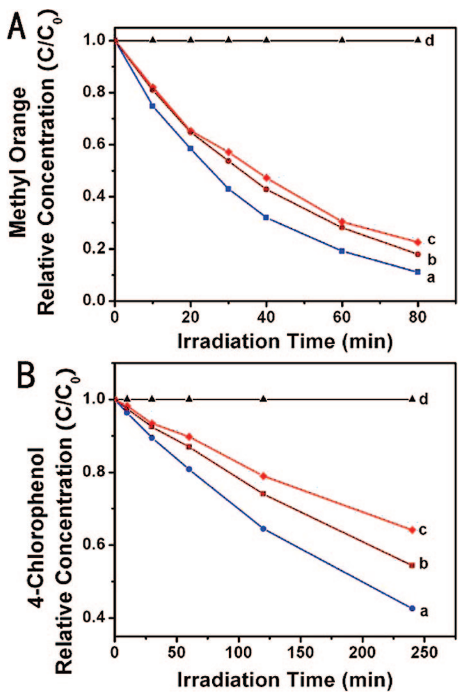

Figure 10. (A) Photodegradation of methyl orange in the presence of (a) ZnO nanowires, (b) ZnO nanoparticles, (c) ZnO bulk, and (d) a blank control. (B) Photodegradation of 4-chlorophenol in the presence of (a) α-Fe_2O_3 nanotubes, (b) α-Fe_2O_3 nanoparticles, (c) α-Fe_2O_3 bulk, and (d) a blank control.

10A. Our nanowire samples exhibited a slightly higher photoactivity as compared with that of both bulk and nanoparticle samples and that observed enhancement of photocatalytic activity is most likely related to a relative increase in the purity and crystallinity of our nanowires. Moreover, because the absorption spectrum of ZnO nanowires is shifted to higher energy with respect to that of the bulk as well as of commercial nanoparticles, the corresponding increase in sensitivity of our nanowires toward that part of the optical spectrum may also account for the larger amount of associated photoactivity noted.[68] Similar morphology-dependent trends in photocatalytic behavior have been previously reported for anatase TiO_2.[69] A similar enhancement of photocatalytic activity was also observed for as-prepared α-Fe_2O_3 nanotubes as compared with that of the nanoparticles and bulk in the decomposition reaction[83] of 4-chlorophenol (4-CP) to CO_2, H_2O, and HCl on the basis of changes in the intensity of the 4-CP absorption peak at 225 nm (Figure 10B).

We determined that both of these photodegradation reactions were pseudo-first-order reactions. From our data in Figure S5, we calculated apparent reaction rate constants of methyl orange degradation for ZnO nanowires, nanoparticles, and the corresponding bulk samples to be 2.77×10^{-2}, 2.13×10^{-2}, and 1.92×10^{-2} min^{-1}, respectively. By analogy, rate constants for the photocatalytic degradation reaction of 4-chlorophenol by α-Fe_2O_3 nanotubes, nanoparticles, and the corresponding bulk samples were deduced to be 3.60×10^{-3}, 2.49×10^{-3}, and 1.86×10^{-3} min^{-1}, respectively.

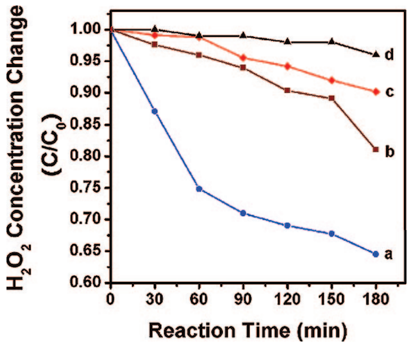

Figure 11. Degradation of H_2O_2 in the presence of (a) CuO nanowires, (b) CuO nanoparticles, (c) CuO bulk, and (d) a blank control.

Degradation of Hydrogen Peroxide. Metal oxides are known to effectively catalyze the degradation of H_2O_2, a model compound for the degradation of organic species.[84] The effect of CuO in catalyzing the degradation of H_2O_2 through a heterogeneous process is shown in Figure 11. It was found that the concentration of H_2O_2 decreased much more quickly in the presence of CuO nanowires and nanoparticles as compared with that of the CuO bulk. In fact, after 3 h of reaction, we noted an approximately 35% and 19% loss of H_2O_2 with CuO nanowires and nanoparticles, respectively, as compared with only a 10% reduction of hydrogen peroxide in the presence of bulk CuO. The small, observed enhancement of photocatalytic activity of our nanowires, relative to that of both commercial bulk and nanoparticle samples, may be related to a rise in CuO crystallinity and chemical purity, characteristic of our as-prepared nanostructures.

CONCLUSIONS

The modified template technique we have developed allows for reasonably short reactions to be run under mild, ambient conditions in aqueous solution with reliable control over shape, dimensionality, and crystallinity, originating from the spatial geometry of the confining porous template environment. We have highlighted the potential of the technique herein to the reliable and reproducible synthesis of not only isolated structures (measuring 50−200 nm in diameter and several micrometers in length) but also of arrays of ZnO, CuO, and α-Fe_2O_3 over spatially relevant, macroscopic (cm^2) areas of various types of substrates (*i.e.*, not only flat silicon surfaces but also curved glass rods). In addition, size- and shape-dependent optical, magnetic, and catalytic properties of these as-prepared 1D metal oxides were investigated and noted to be mainly comparable with or better than the associated properties of the corresponding bulk oxides.

Moreover, we have also proposed plausible explanations for the formation of nanotube and nanowire formulations of the same material under different sets of experimental conditions. That is, it is possible to control morphology by tuning the nature of the physicochemical interactions between reagent molecules and the pore walls, for instance, either (i) by chemically modifying the hydrophilicity, hydrophobicity, and surface charge of the internal pore sidewalls or (ii) by physically altering reagent concentrations, reaction pH, reaction temperatures, and reaction times. This is a particularly advantageous strategy when the metal oxide nanoscale material is difficult to generate by other conventional means.

EXPERIMENTAL SECTION

Synthesis. Commercially available polycarbonate (PC) membranes (Millipore Co.) used in this study contained pore sizes of 50, 100, and 200 nm in diameter, respectively. These polycarbonate filters possess track-etched channels with pores randomly distributed across the filter membranes. Commercially available alumina (AAO) templates (Whatman Co., U.K.) used in this study maintained pore sizes of 200 nm in diameter.

To synthesize ZnO and CuO nanowires, a typical PC membrane was mounted between the two halves of a U-tube cell. The half-cells were then filled with equimolar solutions (0.1 M) of metal salt solutions (*e.g.*, $ZnCl_2$ (Aldrich) for ZnO and $Cu(NO_3)_2$ (Alfa Aesar) for CuO, respectively) and NaOH (Fisher) in water, respectively. The entire U-tube cell was subsequently placed in a water bath whose temperature was set at 80 °C. It has been previously shown[41,42,85,86] that under these experimental conditions, metal hydroxides (such as $Zn(OH)_2$ and $Cu(OH)_2$, in this example) initially form and then transform *via* a low temperature "dehydration" and subsequent crystallization process to ultimately yield their corresponding metal oxides (such as ZnO and CuO, in this case) upon low-temperature heating of the alkaline solution containing these species. Our results for CuO, in particular, visually confirmed this scenario as we were able to observe a change from the blue hue characteristic of $Cu(OH)_2$, initially generated at room temperature, to the coal black color associated with the CuO product in solution, upon heating to 80 °C. After 30 min of reaction, the PC template was detached, thoroughly washed by distilled water, and ultimately removed by immersion in methylene chloride for 10 min. Isolated nanoscale metal oxide samples were then centrifuged, washed with ethanol and distilled water, and finally oven-dried at 80 °C for 24 h.

To synthesize α-Fe_2O_3 nanotubes, an AAO membrane was mounted, as opposed to a PC template, between the two halves of a U-tube cell. The half-cells were then filled with equimolar solutions (0.01 M) of $Fe_2(SO_4)_3$ (J.T. Baker) and ammonium hydroxide (Fisher) in water. The U-tube cell was maintained at room temperature. After 1 h of reaction to prepare $Fe(OH)_3$,[87] the AAO template containing the product was detached, thoroughly washed with distilled water, and oven-dried at 80 °C for 1 h. The AAO template was subsequently annealed at 600 °C for 60 min to ultimately generate α-Fe_2O_3 nanostructures. We note that we were unable to synthesize crystalline hematite, despite numerous experimental variations, without an annealing step. After annealing, the template was removed by immersion in 1 M NaOH for 1 h. Samples were then centrifuged, washed with distilled water until the pH of the solution attained a value of 7, and ultimately oven-dried at 80 °C for 24 h.

It should be noted that, whereas in every case for ZnO, CuO, and α-Fe_2O_3 nanostructures, we are able to generate essentially 100% pure samples in all of our runs, we are still in the process of optimizing overall yields of $<$50%.

Characterization. ***X-ray Diffraction (XRD).*** Crystallographic information on as-prepared samples was obtained using powder XRD through the mediation of a Scintag diffractometer, operating in the Bragg configuration using Cu Kα radiation ($\lambda = 1.54$ Å). Samples for analyses were prepared by grinding powders thoroughly in ethanol using a mortar and pestle, followed by loading onto glass slides and subsequent drying in air. Diffraction patterns were collected from 20 to 80° at a scanning rate of 0.3°/min with a step size of 0.02°. Parameters used for slit widths and accelerating voltages were identical for all samples.

Electron Microscopy. The diameters and lengths of as-prepared nanowires/tubes were initially characterized using a field emission scanning electron microscopy instrument (FE-SEM Leo 1550), operating at an accelerating voltage of 15 kV and equipped with energy-dispersive X-ray spectroscopy (EDS) capabilities. Samples were first dispersed in ethanol, then sonicated for 1 min, and finally deposited onto Si wafers, which were ultimately attached onto the surfaces of SEM brass stubs using conductive carbon tape. Samples were then conductively coated with gold by sputtering for 20 s, so as to minimize charging effects under SEM imaging conditions.

For the creation of nanowire/nanotube arrays, membranes were initially attached to a piece of either double-sided conductive carbon tape or copper tape. The resulting aligned nanowire samples were created by immersion in either 1 M NaOH solution (for AAO membranes) for 0.5 h or in methylene chloride solution (for PC membranes) for 5 min to dissolve and remove the template. After washing steps with distilled water followed by air-drying, samples were subsequently mounted onto a variety of substrates for imaging.

Specimens for transmission electron microscopy (TEM) and high-resolution TEM (HRTEM) were obtained by drying droplets of as-prepared samples from an ethanolic dispersion, which had been sonicated for 1 min, onto a 300 mesh Cu grid, coated with a lacey carbon film. TEM images were then taken at an accelerating voltage of 120 kV on a Philips CM12 instrument. HRTEM images and SAED patterns were obtained on a JEOL 2010F HRTEM at an accelerating voltage of 200 kV. This instrument was equipped with an Oxford INCA EDS system with the potential of performing SAED to further characterize the crystallinity of as-prepared samples.

Photoluminescence (PL). Photoluminescence data were obtained at 25 °C on a Jobin Yvon Spex Fluorolog 3 with a 1 s integration time. PL spectra for ZnO nanowires in water solution were obtained at an excitation wavelength of 325 nm. Prior to data collection, the nanowire solution was sonicated for approximately 30 s to obtain a visually nonscattering dispersion. Fluorescence data were taken immediately afterward.

Ultraviolet−Visible Spectra (UV−vis). UV−visible spectra were obtained at high resolution on a Thermospectronics UV1 spectrometer using quartz cells with a 10-mm path length. UV−visible absorption spectra were recorded using methanol as a blank.

Infrared Spectroscopy (IR). Mid-infrared spectra were recorded by using a Nicolet Nexus 470 FTIR spectrometer with a resolution of 4 cm^{-1}. Solid samples were prepared using a potassium bromide (KBr) pellet.

Photocatalytic Activity. To test the photocatalytic efficiency of as-prepared ZnO nanowires, a solution mixture of 10 mg/L methyl orange containing 1 g/L of ZnO nanowires in water was prepared. Prior to irradiation, the suspensions were sonicated for 10 min and then magnetically stirred in the dark for 30 min to establish an adsorption/degradation equilibrium. The suspension was subsequently irradiated under UV light (emission wavelength maximum at 366 nm) at a $\sim$5 cm separation distance. Analogous control experiments were performed either without ZnO (blank) or in the presence of either a commercial bulk or a commercial nanoparticle (Nanostructured & Amorphous Materials, Inc., 20 nm) sample, normalized for identical metal oxide concentrations. Concentrations of methyl orange in the supernatant aliquots were subsequently analyzed by measuring the absorbance at 464 nm using a Thermospectronics UV1 spectrometer with 10-mm path length quartz cells.

For hematite nanotubes, a similar protocol was utilized with the exception that 4-chlorophenol (4-CP) was tested as opposed to methyl orange. Our source for 20−50 nm commercial hematite nanoparticles was Nanostructured & Amorphous Materials, Inc. The concentration of 4-CP utilized was 6 mg/L and the amount of catalyst loading was set at 50 mg/L. The process for testing the photocatalytic efficiency of hematite nanotubes was essentially identical to the one for ZnO nanowires with the exception that absorbance was measured at an emission wavelength maximum of 225 nm.

Degradation of Hydrogen Peroxide. To probe the ability of as-prepared CuO nanowires to catalyze the degradation of H_2O_2, a 20 mL solution mixture containing 0.6 M H_2O_2 and 0.5 g/L CuO nanowires was initially prepared with rapid magnetic stirring. A 1 mL portion was removed every 30 min and the concentration of H_2O_2 in the subsequent pH-adjusted supernatant aliquots was subsequently analyzed by titration with a solution of 0.02 M $KMnO_4$.[88] Analogous control experiments were performed either without CuO (blank) or in the presence of either a commercial bulk or a commercial nanoparticle (Nanostructured & Amorphous Materials, Inc., 30−50 nm) sample, normalized for identical metal oxide concentrations.

SQUID. Magnetization measurements were obtained using a Quantum Design magnetic property measurement system (MPMS) superconducting quantum interference device (SQUID) magnetometer, operated over a temperature range of 5−300 K, at an applied field of 100 Oe. Magnetization *versus* applied field measurements were obtained using **H** values from −5000 to 5000 Oe. Powder samples of as-prepared products were pressed lightly, loaded into a gel cap, and then covered with silica wool. The sample was held within a uniform drinking straw, which was attached to the sample rod of the MPMS apparatus. Signals generated by measurements of an empty sample holder demonstrated that the holder assembly contributes <1% to the overall magnetic signal.

Acknowledgment. We acknowledge the U.S. Department of Energy (Grant DE-AC02-98CH10886) for facility and personnel support. We also thank the National Science Foundation (CAREER Award DMR-0348239), and the Alfred P. Sloan Foundation (2006–2008) for PI support and experimental supplies. Moreover, we are grateful to D. Wang (Boston College) as well as to S. van Horn and J. Quinn (SUNY Stony Brook) for their assistance with electron microscopy. In addition, we thank Q. Li and Q. Jie (Brookhaven National Laboratory) for their assistance with SQUID measurements.

Supporting Information Available: Table S1 tabulates K_{sp} values at 25 °C for as-generated metal hydroxides. Figure S1 is a schematic of the experimental setup used to synthesize metal oxide nanostructures. Figures S2−S3 contain additional SEM and TEM images of samples. Figure S4 illustrates FT-IR spectra of as-prepared nanoscale samples of various metal oxides. Figure S5 contains additional photocatalytic degradation data for ZnO and hematite samples. This material is available free of charge *via* the Internet at http://pubs.acs.org.

REFERENCES AND NOTES

1. Hu, J.; Odom, T. W.; Lieber, C. M. Chemistry and Physics in One Dimension: Synthesis and Properties of Nanowires and Nanotubes. *Acc. Chem. Res.* **1999**, *32*, 435–445.
2. Iijima, S. Helical Microtubules of Graphitic Carbon. *Nature* **1991**, *354*, 56–58.
3. Holmes, J. D.; Johnston, K. P.; Doty, R. C.; Korgel, B. A. Control of Thickness and Orientation of Solution-Grown Silicon Nanowires. *Science* **2000**, *287*, 1471–1473.
4. Arakawa, Y.; Sakaki, H. Multidimensional Quantum Well Laser and Temperature Dependence of Its Threshold Current. *Appl. Phys. Lett.* **1982**, *40*, 939–941.
5. Cui, Y.; Lieber, C. M. Functional Nanoscale Electronic Devices Assembled Using Silicon Nanowire Building Blocks. *Science* **2001**, *291*, 851–853.
6. Huang, M. H.; Mao, S.; Feick, H.; Yan, H.; Wu, Y.; Kind, H.; Webber, E.; Russo, R.; Yang, P. Room-Temperature Ultraviolet Nanowire Nanolasers. *Science* **2001**, *292*, 1897–1899.
7. Xia, Y.; Yang, P.; Sun, Y.; Wu, Y.; Mayers, B.; Gates, B.; Yin, Y.; Kim, F.; Yan, H. One-Dimensional Nanostructures: Synthesis, Characterization, and Applications. *Adv. Mater.* **2003**, *15*, 353–389.
8. Fan, Z.; Wang, D.; Chang, P.-C.; Tseng, W.-Y.; Lu, J. G. ZnO Nanowire Field-Effect Transistor and Oxygen Sensing Property. *Appl. Phys. Lett.* **2004**, *85*, 5923–5925.
9. Johnson, J. C.; Knutsen, K. P.; Yan, H.; Law, M.; Zhang, Y.; Yang, P.; Saykally, R. J. Ultrafast Carrier Dynamics in Single ZnO Nanowire and Nanoribbon Lasers. *Nano Lett.* **2004**, *4*, 197–204.
10. Law, M.; Greene, L. E.; Radenovic, A.; Kuykendall, T.; Liphardt, J.; Yang, P. ZnO-Al_2O_3 and ZnO-TiO_2 Core-Shell Nanowire Dye-Sensitized Solar Cells. *J. Phys. Chem. B* **2006**, *110*, 22652–22663.
11. Johnson, J. C.; Yan, H.; Schaller, R. D.; Harber, L. H.; Saykally, R. J.; Yang, P. Single Nanowire Lasers. *J. Phys. Chem. B* **2001**, *105*, 11387–11390.
12. Law, M.; Greene, L. E.; Johnson, J. C.; Saykally, R.; Yang, P. Nanowire Dye-Sensitized Solar Cells. *Nat. Mater.* **2005**, *4*, 455–459.
13. Sun, Z.; Yuan, H.; Liu, Z.; Han, B.; Zhang, X. A Highly Efficient Chemical Sensor Material for H_2S: α-Fe_2O_3 Nanotubes Fabricated Using Carbon Nanotube Templates. *Adv. Mater.* **2005**, *17*, 2993–2997.
14. Chen, J.; Xu, L.; Li, W.; Gou, X. α-Fe_2O_3 Nanotubes in Gas Sensor and Lithium-Ion Battery Applications. *Adv. Mater.* **2005**, *17*, 582–586.
15. Zhu, Y. W.; Yu, T.; Cheong, F. C.; Xu, X. J.; Lim, C. T.; Tan, V. B. C.; Thong, J. T. L.; Sow, C. H. Large-Scale Synthesis and Field Emission Properties of Vertically Oriented CuO Nanowire Films. *Nanotechnology* **2005**, *16*, 88–92.
16. Reynolds, D. C.; Look, D. C.; Jogai, B.; Litton, C. W.; Collins, T. C.; Harsch, W.; Cantwell, G. Neutral-Donor-Bound-Exciton Complexes in ZnO Crystals. *Phys. Rev. B* **1998**, *57*, 12151–12155.
17. Kind, H.; Yan, H.; Messer, B.; Law, M.; Yang, P. Nanowire Ultraviolet Photodetectors and Optical Switches. *Adv. Mater.* **2002**, *14*, 158–160.
18. Soci, C.; Zhang, A.; Xiang, B.; Dayeh, S. A.; Aplin, D. P. R.; Park, J.; Bao, X. Y.; Lo, Y. H.; Wang, D. ZnO Nanowire UV Photodetectors with High Internal Gain. *Nano Lett.* **2007**, *7*, 1003–1009.
19. Suh, D.-I.; Lee, S.-Y.; Kim, T.-H.; Chun, J.-M.; Suh, E.-K.; Yang, O.-B.; Lee, S.-K. The Fabrication and Characterization of Dye-Sensitized Solar Cells with a Branched Structure of ZnO Nanowires. *Chem. Phys. Lett.* **2007**, *442*, 348–353.
20. Goldberger, J.; Sirbuly, D. J.; Law, M.; Yang, P. ZnO Nanowire Transistors. *J. Phys. Chem. B* **2005**, *109*, 9–14.
21. Noh, Y.-Y.; Cheng, X.; Sirringhaus, H.; Sohn, J. I.; Welland, M. E.; Kang, D. J. Ink-Jet Printed ZnO Nanowire Field Effect Transistors. *Appl. Phys. Lett.* **2007**, *91*, 043109-1−043109-3.
22. Wang, X.; Zhou, J.; Lao, C.; Song, J.; Xu, N.; Wang, Z. L. In Situ Field Emission of Density-Controlled ZnO Nanowire Arrays. *Adv. Mater.* **2007**, *19*, 1627–1631.
23. Wang, Z. L.; Song, J. Piezoelectric Nanogenerators Based on Zinc Oxide Nanowire Arrays. *Science* **2006**, *312*, 242–246.
24. Gao, P. X.; Song, J.; Liu, J.; Wang, Z. L. Nanowire Piezoelectric Nanogenerators on Plastic Substrates as Flexible Power Sources for Nanodevices. *Adv. Mater.* **2007**, *19*, 67–72.
25. Wang, X.; Liu, J.; Song, J.; Wang, Z. L. Integrated Nanogenerators in Biofluid. *Nano Lett.* **2007**, *7*, 2475–2479.
26. Park, W. I.; Yi, G.-C.; Kim, M.; Pennycook, S. J. ZnO Nanoneedles Grown Vertically on Si Substrates by Non-Catalytic Vapor-Phase Epitaxy. *Adv. Mater.* **2002**, *14*, 1841–1843.
27. Jeong, M.-C.; Oh, B.-Y.; Nam, O.-H.; Kim, T.; Myoung, J.-M. Three-Dimensional ZnO Hybrid Nanostructures for Oxygen Sensing Application. *Nanotechnology* **2006**, *17*, 526–530.
28. Yang, P.; Han, H.; Mao, S.; Russo, R.; Johnson, J.; Saykally, R.; Morris, N.; Pham, J.; He, R.; Choi, H.-J. Controlled Growth of ZnO Nanowires and Their Optical Properties. *Adv. Funct. Mater.* **2002**, *12*, 323–331.

29. Umar, A.; Kim, B.-K.; Kim, J.-J.; Hahn, Y. B. Optical and Electrical Properties of ZnO Nanowires Grown on Aluminium Foil by Non-Catalytic Thermal Evaporation. *Nanotechnology* **2007**, *18*, 175606-1−175606-7.
30. Sun, Y.; Fuge, G. M.; Ashfold, M. N. R. Growth of Aligned ZnO Nanorod Arrays by Catalyst-Free Pulsed Laser Deposition Methods. *Chem. Phys. Lett.* **2004**, *396*, 21–26.
31. Vayssieres, L. Growth of Arrayed Nanorods and Nanowires of ZnO from Aqueous Solutions. *Adv. Mater.* **2003**, *15*, 464–466.
32. Greene, L. E.; Law, M.; Goldberger, J.; Kim, F.; Johnson, J. C.; Zhang, Y.; Saykally, R. J.; Yang, P. Low-Temperature Wafer-Scale Production of ZnO Nanowire Arrays. *Angew. Chem., Int. Ed.* **2003**, *42*, 3031–3034.
33. Greene, L. E.; Law, M.; Tan, D. H.; Montano, M.; Goldberger, J.; Somorjai, G.; Yang, P. General Route to Vertical ZnO Nanowire Arrays Using Textured ZnO Seeds. *Nano Lett.* **2005**, *5*, 1231–1236.
34. Jiang, X.; Herricks, T.; Xia, Y. CuO Nanowires Can Be Synthesized by Heating Copper Substrates in Air. *Nano Lett.* **2002**, *2*, 1333–1338.
35. Musa, A. O.; Akomolafe, T.; Carter, M. J. Production of Cuprous Oxide, A Solar Cell Material, by Thermal Oxidation and A Study of Its Physical and Electrical Properties. *Sol. Energy Mater. Sol. Cells* **1998**, *51*, 305–316.
36. Reitz, J. B.; Solomon, E. I. Propylene Oxidation on Copper Oxide Surfaces: Electronic and Geometric Contributions to Reactivity and Selectivity. *J. Am. Chem. Soc.* **1998**, *120*, 11467–11478.
37. Lanza, F.; Feduzi, R.; Fuger, J. Effects of Lithium Oxide on the Electrical Properties of CuO at Low Temperatures. *J. Mater. Res.* **1990**, *5*, 1739–1744.
38. Podhájecký, P.; Zábranský, Z.; Novák, P.; Dobiášová, Z.; Èerný, R.; Valvoda, V. Relation Between Crystallographic Microstructure and Electrochemical Properties of CuO for Lithium Cells. *Electrochim. Acta* **1990**, *35*, 245–249.
39. Cheng, C.-L.; Ma, Y.-R.; Chou, M. H.; Huang, C. Y.; Yeh, V.; Wu, S. Y. Direct Observation of Short-Circuit Diffusion during the Formation of A Single Cupric Oxide Nanowire. *Nanotechnology* **2007**, *18*, 245604-1−245604-5.
40. Cao, M.; Hu, C.; Wang, Y.; Guo, Y.; Guo, C.; Wang, E. A Controllable Synthetic Route to Cu, Cu_2O, and CuO Nanotubes and Nanorods. *Chem. Commun.* **2003**, 1884–1885.
41. Wen, X.; Xie, Y.; Choi, C. L.; Wan, K. C.; Li, X.-Y.; Yang, S. Copper-Based Nanowire Materials: Templated Syntheses, Characterizations, and Applications. *Langmuir* **2005**, *21*, 4729–4737.
42. Du, G. H.; Tendeloo, G. V. $Cu(OH)_2$ Nanowires, CuO Nanowires and CuO Nanobelts. *Chem. Phys. Lett.* **2004**, *393*, 64–69.
43. Lu, C.; Qi, L.; Yang, J.; Zhang, D.; Wu, N.; Ma, J. Simple Template-Free Solution Route for the Controlled Synthesis of $Cu(OH)_2$ and CuO Nanostructures. *J. Phys. Chem. B* **2004**, *108*, 17825–17831.
44. Zhang, W.; Ding, S.; Yang, Z.; Liu, A.; Qian, Y.; Tang, S.; Yang, S. Growth of Novel Nanostructured Copper Oxide (CuO) Films on Copper Foil. *J. Cryst. Growth* **2006**, *291*, 479–484.
45. Wu, H.; Lin, D.; Pan, W. Fabrication, Assembly, and Electrical Characterization of CuO Nanofibers. *Appl. Phys. Lett.* **2006**, *89*, 133125-1−133125-3.
46. Malandrino, G.; Finocchiaro, S. T.; Nigro, R. L.; Bongiorno, C.; Spinella, C.; Fragalà, I. L. Free-Standing Copper(II) Oxide Nanotube Arrays through an MOCVD Template Process. *Chem. Mater.* **2004**, *16*, 5559–5561.
47. Yi-Kun, S.; Cheng-Min, S.; Hai-Tao, Y.; Hu-Lin, L.; Hong-Jun, G. Controlled Synthesis of Highly Ordered CuO Nanowire Arrays by Template-Based Sol-Gel Route. *Trans. Nonferrous Met. SOC. China* **2007**, *17*, 783–786.
48. Gondal, M. A.; Hameed, A.; Yamani, Z. H.; Suwaiyan, A. Laser induced photo-catalytic oxidation/splitting of water over α-Fe_2O_3, WO_3, TiO_2 and NiO catalysts: activity comparison. *Chem. Phys. Lett.* **2004**, *385*, 111–115.
49. Ohmori, T.; Takahashi, H.; Mametsuka, H.; Suzuki, E. Photocatalytic Oxygen Evolution on α-Fe_2O_3 Films Using Fe^{3+} Ion as a Sacrificial Oxidizing Agent. *Phys. Chem. Chem. Phys.* **2000**, *2*, 3519–3522.
50. Fu, Y. Y.; Wang, R. M.; Xu, J.; Chen, J.; Yan, Y.; Narlikar, A. V.; Zhang, H. Synthesis of Large Arrays of Aligned α-Fe_2O_3 Nanowires. *Chem. Phys. Lett.* **2003**, *379*, 373–379.
51. Wen, X.; Wang, S.; Ding, Y.; Wang, Z. L.; Yang, S. Controlled Growth of Large-Area, Uniform, Vertically Aligned Arrays of r-Fe_2O_3 Nanobelts and Nanowires. *J. Phys. Chem. B* **2005**, *109*, 215–220.
52. Wang, X.; Chen, X.; Gao, L.; Zheng, H.; Ji, M.; Tang, C.; Shen, T.; Zhang, Z. Synthesis of β-FeOOH and α-Fe_2O_3 Nanorods and Electrochemical Properties of β-FeOOH. *J. Mater. Chem.* **2004**, *14*, 905–907.
53. Xiong, Y.; Li, Z.; Li, X.; Hu, B.; Xie, Y. Thermally Stable Hematite Hollow Nanowires. *Inorg. Chem.* **2004**, *43*, 6540–6542.
54. Morber, J. R.; Ding, Y.; Haluska, M. S.; Li, Y.; Liu, J. P.; Wang, Z. L.; Snyder, R. L. PLD-Assisted VLS Growth of Aligned Ferrite Nanorods, Nanowires, and Nanobelts-Synthesis, and Properties. *J. Phys. Chem. B* **2006**, *110*, 21672–21679.
55. Shen, X.-P.; Liu, H.-J.; Pan, L.; Chen, K.-M.; Hong, J.-M.; Xu, Z. An Efficient Template Pathway to Synthesis of Ordered Metal Oxide Nanotube Arrays Using Metal Acetylacetonates as Single-Source Molecular recursors. *Chem. Lett.* **2004**, *33*, 1128–1129.
56. Hulteen, J. C.; Martin, C. R. A General Template-Based Method for the Preparation of Nanomaterials. *J. Mater. Chem.* **1997**, *7*, 1075–1087.
57. Martin, C. R. *Nanomaterials: A Membrane-Based Synthetic Approach Science* **1994**, *266*, 1961–1966.
58. Martin, C. R. Membrane-Based Synthesis of Nanomaterials. *Chem. Mater.* **1996**, *8*, 1739–1746.
59. Mao, Y.; Wong, S. S. General, Room-Temperature Method for the Synthesis of Isolated as Well as Arrays of Single-Crystalline ABO_4-Type Nanorods. *J. Am. Chem. Soc.* **2004**, *126*, 15245–15252.
60. Mao, Y.; Zhang, F.; Wong, S. S. Ambient Template-Directed Synthesis of Single-Crystalline Alkaline-Earth Metal Fluoride Nanowires. *Adv. Mater.* **2006**, *18*, 1895–1899.
61. Martin, C. R.; Dyke, L. S. V.; Cai, Z.; Liang, W. Template Synthesis of Organic Microtubules. *J. Am. Chem. Soc.* **1990**, *112*, 8976–8977.
62. Liang, W.; Martin, C. R. Gas Transport in Electronically Conductive Polymers. *Chem. Mater.* **1991**, *3*, 390–391.
63. Cochran, R. E.; Shyue, J.-J.; Padture, N. P. Template-Based, Near-Ambient Synthesis of Crystalline Metal-Oxide Nanotubes, Nanowires and Coaxial Nanotubes. *Acta Mater.* **2007**, *55*, 3007–3014.
64. Prasad, V.; D'Souza, C.; Yadav, D.; Shaikh, A. J.; Vigneshwaran, N. Spectroscopic Characterization of Zinc Oxide Nanorods Synthesized by Solid-State Reaction. *Spectrochim. Acta, Part A* **2006**, *65*, 173–178.
65. Snitka, V.; Jankauskas, V.; Zunda, A.; Mizariene, V. Deposition of Nanocrystalline ZnO by Wire Explosion Technique and Characterization of the Films' Properties. *Mater. Lett.* **2007**, *61*, 1763–1766.
66. Wang, S.-B.; Min, Y.-L.; Yu, S.-H. Synthesis and Magnetic Properties of Uniform Hematite Nanocubes. *J. Phys. Chem. C* **2007**, *111*, 3551–3554.
67. Kaur, M.; Muthe, K. P.; Despande, S. K.; Choudhury, S.; Singh, J. B.; Verma, N.; Gupta, S. K.; Yakhmi, J. V. Growth and Branching of CuO Nanowires by Thermal Oxidation of Copper. *J. Cryst. Growth* **2006**, *289*, 670–675.
68. Zhou, H.; Park, T.-J.; Wong, S. S. Synthesis, Characterization, and Photocatalytic Properties of Pyrochlore $Bi_2Ti_2O_7$ Nanotubes. *J. Mater. Res.* **2006**, *21*, 2941–2947.
69. Mao, Y.; Wong, S. S. Size- and Shape-Dependent Transformation of Nanosized Titanate into Analogous Anatase Titania Nanostructures. *J. Am. Chem. Soc.* **2006**, *128*, 8217–8226.
70. Huang, M. H.; Wu, Y.; Feick, H.; Tran, N.; Weber, E.; Yang, P. Catalytic Growth of Zinc Oxide Nanowires by Vapor Transport. *Adv. Mater.* **2001**, *13*, 113–116.

71. Vanheusden, K.; Warren, W. L.; Seager, C. H.; Tallant, D. R.; Voigt, J. A.; Gnade, B. E. Mechanisms Behind Green Photoluminescence in ZnO Phosphor Powders. *J. Appl. Phys.* **1996**, *79*, 7983–7990.
72. Maensiri, S.; Laokul, P.; Promarak, V. Synthesis and Optical Properties of Nanocrystalline ZnO Powders by A Simple Method Using Zinc Acetate Dihydrate and Poly(vinyl pyrrolidone). *J. Cryst. Growth* **2006**, *289*, 102–106.
73. Xiong, G.; Pal, U.; Serrano, J. G. Correlations among Size, Defects, and Photoluminescence in ZnO Nanoparticles. *J. Appl. Phys.* **2007**, *101*, 024317-1−024317-6.
74. Kaschner, A.; Haboeck, U.; Strassburg, M.; Strassburg, M.; Kaczmarczyk, G.; Hoffmann, A.; Thomsen, C.; Zeuner, A.; H. R; Alves, D. M. H.; Meyer, B. K. Nitrogen-related Local Vibrational Modes in ZnO:N. *Appl. Phys. Lett.* **2002**, *80*, 1909–1911.
75. Amores, J. M. G.; Escribano, V. S.; Busca, G.; Lorenzelli, V. Solid-State and Surface Chemistry of CuO-TiO_2 (Anatase) Powders. *J. Mater. Chem.* **1994**, *4*, 965–971.
76. Borgohain, K.; Singh, J. B.; Rao, M. V. R.; Shripathi, T.; Mahamuni, S. Quantum Size Effects in CuO Nanoparticles. *Phys. Rev. B* **2000**, *61*, 11093–11096.
77. Wang, Y.; Muramatsu, A.; Sugimoto, T. FTIR Analysis of Well-Defined α-Fe_2O_3 particles. *Colloids Surf., A* **1998**, *134*, 281–297.
78. Musić, S.; Czako-Nagy, I.; Salaj-Obelić, I.; Ljubešić, N. Formation of α-Fe_2O_3 Particles in Aqueous Medium and Their Properties. *Mater. Lett.* **1997**, *32*, 301–305.
79. Chernyshova, I. V.; Hochella, M. F.; Madden, A. S. Size-dependent Structural Transformations of Hematite Nanoparticles. 1.Phase Transition. *Phys. Chem. Chem. Phys.* **2007**, *9*, 1736–1750.
80. Morin, F. J. Magnetic Susceptibility of α-Fe_2O_3 and α-Fe_2O_3 with Added Titanium. *Phys. Rev.* **1950**, *78*, 819–820.
81. Liu, L.; Kou, H.-Z.; Mo, W.; Liu, H.; Wang, Y. Surfactant-Assisted Synthesis of α-Fe_2O_3 Nanotubes and Nanorods with Shape-Dependent Magnetic Properties. *J. Phys. Chem. B* **2006**, *110*, 15218–15223.
82. Zysler, R. D.; Winkler, E.; Mansilla, M. V.; Fiorani, D. Surface Effect in the Magnetic Order of Antiferromagnetic Nanoparticles. *Physica B* **2006**, *384*, 277–281.
83. Bandara, J; Klehm, U.; J, K. Raschig Rings-Fe_2O_3 Composite Photocatalyst Activate in the Degradation of 4-Chlorophenol and Orange II under Daylight Irradiation. *Appl. Catal., B* **2007**, *76*, 73–81.
84. Drijvers, D.; Langenhove, H. V.; Beckers, M. Decomposition of Phenol and Trichloroethylene by the Ultrasound/H_2O_2/CuO Process. *Water Res.* **1999**, *33*, 1187–1194.
85. Uekawa, N.; Iahii, S.; Kojima, T.; Kakegawa, K. Formation of Porous Spherical Aggregated Structure of ZnO Nanoparticles by Low-Temperature Heating of $Zn(OH)_2$ in Diol Solution. *Mater. Lett.* **2007**, *61*, 1729–1734.
86. Ullah, M. H.; Kim, I.; Ha, C.-S. One-Step Synthetic Route for Producing Nanoslabs: Zn-Oriented Polycrystalline and Single-Crystalline Zinc Oxide. *J. Mater. Sci.* **2006**, *41*, 3263–3269.
87. Nashaat, N, N.; Maen, M, H. Study and Modeling of Iron Hydroxide Nanoparticle Uptake by AOT (w/o) Microemulsions. *Langmuir* **2007**, *23*, 13093–13103.
88. Klassen, N. V.; Marchington, D.; Mcgowan, H. C. E. H_2O_2 Determination by the I_3^- Method and by $KMnO_4$ Titration. *Anal. Chem.* **1994**, *66*, 2921–2925.